Article

Disorder-assisted assembly of strongly correlated fluids of light

https://doi.org/10.1038/s41586-022-05357-x

Received: 1 July 2022

Accepted: 16 September 2022

Published online: 14 December 2022

Check for updates

Brendan Saxberg[1,5]✉, Andrei Vrajitoarea[1,5], Gabrielle Roberts[1,5], Margaret G. Panetta[1], Jonathan Simon[1,2,3,4] & David I. Schuster[1,3,4]

Guiding many-body systems to desired states is a central challenge of modern quantum science, with applications from quantum computation[1,2] to many-body physics[3] and quantum-enhanced metrology[4]. Approaches to solving this problem include step-by-step assembly[5,6], reservoir engineering to irreversibly pump towards a target state[7,8] and adiabatic evolution from a known initial state[9,10]. Here we construct low-entropy quantum fluids of light in a Bose–Hubbard circuit by combining particle-by-particle assembly and adiabatic preparation. We inject individual photons into a disordered lattice for which the eigenstates are known and localized, then adiabatically remove this disorder, enabling quantum fluctuations to melt the photons into a fluid. Using our platform[11], we first benchmark this lattice melting technique by building and characterizing arbitrary single-particle-in-a-box states, then assemble multiparticle strongly correlated fluids. Intersite entanglement measurements performed through single-site tomography indicate that the particles in the fluid delocalize, whereas two-body density correlation measurements demonstrate that they also avoid one another, revealing Friedel oscillations characteristic of a Tonks–Girardeau gas[12,13]. This work opens new possibilities for the preparation of topological and otherwise exotic phases of synthetic matter[3,14,15].

Synthetic materials, which are composed of interacting ions[16], atoms[17] or photons[3,18], rather than interacting electrons as in solid state materials, offer a unique window into the equilibrium and dynamical properties of many-body quantum systems. Near-equilibrium, minimal realizations of superconductors[19], Mott insulators[20] and topological bands[15,21] have elucidated the essential physics of these materials. Lattice site[22] and time[23] resolved probes have exposed previously inaccessible quantities, such as entanglement[24,25], to direct observation.

Recently, efforts in synthetic matter have begun to explore explicitly out-of-equilibrium phenomena, including time crystallinity[26,27], many-body localization[28,29], quantum scarring[30] and bad-metal transport[31], with prospects for exploring phenomena such as light-induced superconductivity[32] and measurement-induced phase transitions[33]. These experiments have a particularly marked impact on benchmarking computational tools, as late-time dynamics of moderately sized quantum systems are already beyond the capabilities of state-of-the-art numerics[34].

Often neglected is the fact that preparing equilibrium states is itself an intrinsically non-equilibrium process, because driving a quantum many-body system to a desired target state requires 'dynamics'. This challenge is typically overlooked in the solid state, in which thermalization of long-lived electrons with broadband thermal reservoirs enables robust entropy removal despite fundamentally inefficient thermalization. In synthetic materials, limited particle lifetimes make it crucial to develop optimized state preparation schemes that approach the fundamental quantum speed limits.

Efficient preparation of many-body states of ultracold atoms typically involves: (1) laser cooling, in which scattered light removes entropy from individual atoms; (2) evaporative cooling, in which collisions dump entropy into consequently lost atoms, producing a Bose–Einstein condensate (BEC); and (3) adiabatic variation of the Hamiltonian, so that the weakly interacting (BEC) ground state of the initial Hamiltonian evolves into the strongly interacting ground state of the final Hamiltonian. This approach has been used to produce, for example, Mott insulating[20] and magnetically ordered[35,36] synthetic matter.

Materials composed of microwave photons[3] offer the unique possibility of efficient thermalization via coupling to arbitrarily designed low-entropy reservoirs shaped through resonant filters[37]. This approach has been used to stabilize Mott states of light[11], with prospects for devil's staircase[38] and Laughlin-like[39] matter. Such reservoir engineering works extremely well to stabilize incompressible matter; preparation of compressible phases, such as superfluids[40] and certain quantum spin liquids[41], requires new approaches.

In this work we harness another strength of photonic materials platforms—particle-resolved 'control'—to explore a new class of state preparation schemes compatible with compressible matter. Our approach marries the addressability of particle-by-particle injection with the robustness of adiabatic evolution, enabling us to assemble

[1]The Department of Physics and James Frank Institute, University of Chicago, Chicago, IL, USA. [2]The Department of Physics, Stanford University, Stanford, CA, USA. [3]The Department of Applied Physics, Stanford University, Stanford, CA, USA. [4]The Pritzker School of Molecular Engineering, University of Chicago, Chicago, IL, USA. [5]These authors contributed equally: Brendan Saxberg, Andrei Vrajitoarea, Gabrielle Roberts. ✉e-mail: bsaxberg@uchicago.edu

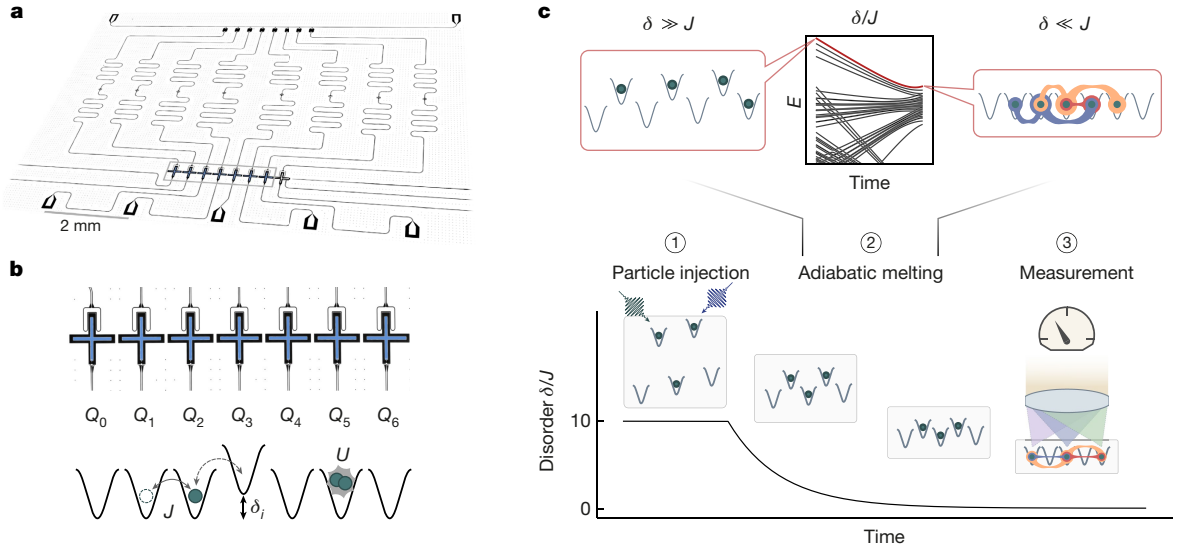

Fig. 1 | Individually addressed many-body states in the Bose–Hubbard circuit. a, The physical system consists of a 1D array of capacitively coupled transmon qubits patterned on a large-area superconducting microwave circuit. This system behaves as a tight-binding lattice for photons[11] with site-resolved readout performed via microwave resonators dispersively coupled to each qubit, and real-time tuning of lattice disorder controlled by inductively coupled flux bias lines. **b**, The physics of this 1D circuit is well characterized by the Bose–Hubbard Hamiltonian describing the dynamics of interacting particles on a lattice. The transmon qubits (highlighted in blue) realize the lattice sites in which the photonic particles reside[50], with intersite tunnelling J arising from their capacitive coupling, and the on-site interaction U stemming from their anharmonicity. The flux bias lines tune the transmon energies to provide site-resolved control over lattice disorder δ_i. **c**, To prepare (near) arbitrary eigenstates of the disorder-free Hubbard lattice, we impose strong ($|\delta_i| \gg |J|$) controlled disorder, ensuring that all eigenstates are products of localized photons on individual sites. (1), In this disordered configuration it is then straightforward to excite an arbitrary eigenstate by injecting photons into individual lattice sites. (2), If the disorder is slowly removed ($|\delta_i| \to 0$), the adiabatic theorem ensures that the system always remains in the same instantaneous many-body eigenstate, resulting in a highly entangled many-body state of the disorder-free lattice. (3) We characterize this many-body state via site-resolved occupation and correlation measurements.

arbitrary-density fluids of strongly interacting microwave photons in our one-dimensional (1D) Bose–Hubbard circuit[11]. We first localize all eigenstates by imposing disorder that is much stronger than the tunnelling. We then inject individual particles into localized lattice orbitals, populating a single- or many-body eigenstate of our choosing. Finally, we adiabatically remove the disorder, melting this localized eigenstate into a strongly correlated fluid via tunnelling-induced quantum fluctuations. To characterize the fidelity of the preparation scheme, we introduce a reversible ramp protocol that maps diabatic and decay-induced excitations of the fluid onto localized excitations in the disordered lattice. We then characterize the fluid in two ways: (1) two-body correlation measurements, which reveal that the photons avoid one another in the fluid phase, with a universal structure characteristic of a Tonks gas; and (2) intersite entanglement measurements, via the purity of single-site density matrices, which reveal that the photons delocalize during the melt and relocalize when disorder is adiabatically re-introduced.

In what follows, we first introduce the Bose–Hubbard circuit platform and its capabilities. We then describe the disorder-localized preparation scheme and test it by assembling arbitrary single-particle quasi-momentum states. We validate adiabaticity of the scheme via the reversibility of the protocol, directly measuring entropy generation in the disordered lattice. We then apply the preparation scheme to assemble few-particle states, characterizing them using new tools which reveal that the particles simultaneously delocalize and anti-bunch, hallmarks of a strongly interacting fluid of light.

The Bose–Hubbard circuit

Our experiments take place in the quantum circuit shown in Fig. 1a, the physics of which is captured by a 1D Bose–Hubbard model for photons (illustrated in Fig. 1b):

$$H_{\mathrm{BH}}/\hbar = J\sum_{\langle i,j\rangle} a_i^\dagger a_j + \frac{U}{2}\sum_i n_i(n_i-1) + \sum_i (\omega_0+\delta_i)n_i.$$

The operator $a_i^\dagger$ (a_i) creates (destroys) a microwave photon on site i, with the number operator on site i given by $n_i = a_i^\dagger a_i$. J is the nearest-neighbour tunnelling rate, U is the on-site interaction energy, $\omega_0 + \delta_i$ is the energy to create the first photon in site i and $\hbar$ is the reduced Planck's constant.

The lattice sites in which the photons reside are realized as transmon qubits[3]. The anharmonicity of the transmon provides the photon–photon interaction on that site. Capacitive coupling between adjacent transmons enables nearest-neighbour tunnelling, and flux loops permit qubit-by-qubit tuning of the on-site energies. We operate with $J/2\pi = 9$ MHz, $U/2\pi = -230$ MHz; note that we have fixed the (otherwise arbitrary) gauge of the Hamiltonian with a tunnelling term whose sign is the opposite convention to compensate for our $U < 0$ and ensure that the highest energy single-particle states have the 'lowest' quasi-momenta. Site frequencies are tunable in real time over $(\omega_0 + \delta_i)/2\pi \in [4.1, 6.1]$ GHz (Methods), enabling introduction of disorder δ_i up to 2 GHz, which is much larger than the tunnelling energy. The photon lifetime in the lattice is $T_1 > 10$ μs, so $|U| \gg J \gg 1/T_1$ providing ample time for the photons to collide, organize and become entangled before decaying (Supplementary Section I). Site-resolved microscopy is achieved by capacitive coupling of each transmon to an off-resonant coplanar waveguide resonator, enabling direct readout of each transmon's occupation number through the dispersive shift of the resonator (Supplementary Sections D and E). Because the system operates in the hard-core limit $|U| \gg J$, the many-body states prepared are expected to be lattice analogues of a Tonks–Girardeau gas of impenetrable bosons[42,43].

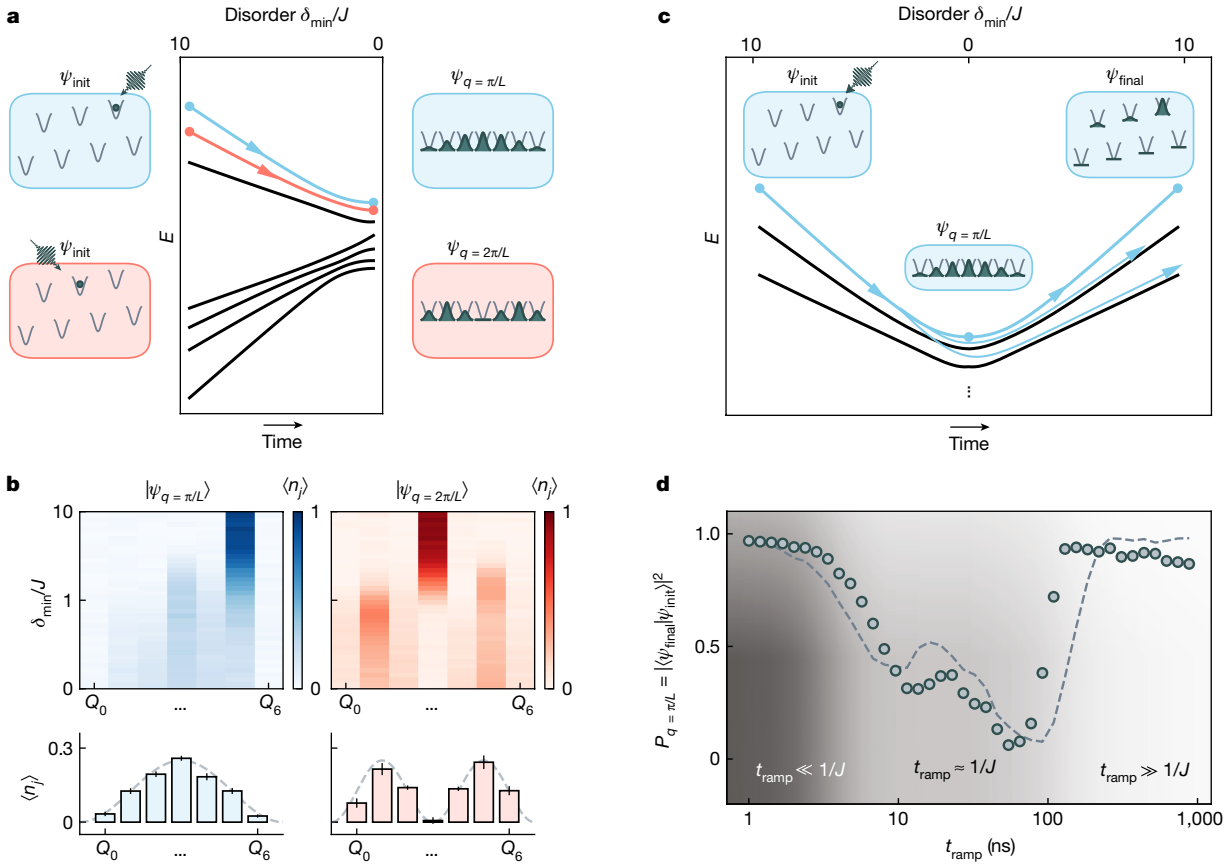

Fig. 2 | Adiabatic assembly of single-particle eigenstates. a–**d**, The simplest demonstration of the preparation protocol is the construction of single-photon particle-in-a-box states. **a**, We plot the numerically computed instantaneous eigenstate energies of a photon in a lattice, as disorder is reduced to zero over time. We highlight the highest (second highest) energy eigenstates in blue (red). In the disordered lattice, the highest (second highest) energy eigenstate is a particle localized to the single highest (second highest) energy site, and, as disorder is decreased, this state is adiabatically transformed into the particle-in-a-box state with lowest (second lowest) quasi-momentum. **b**, We demonstrate this process experimentally by assembling these lowest two quasi-momentum states. The blue (red) plots show the occupation of each of the lattice sites over time, as the disorder is adiabatically reduced to zero; here a single photon initially occupying the highest (second highest) energy site, Q_5 (Q_3) delocalizes into the corresponding quasi-momentum state $q = \pi/L$ ($q = 2\pi/L$), shown at the final time in the bottom panels. **c**, To characterize the time required for the adiabatic sweep, we follow the protocol depicted: (1) a photon is prepared in a particular site in the presence of disorder; (2) the disorder is ramped down and back up over a variable time $2t_{ramp}$; (3) the final occupation of the initially prepared site $|\langle\Psi_{final}|\Psi_{init}\rangle|^2$ is measured. **d**, The result of this protocol for the highest energy state (with dashed parameter-free theory), demonstrates that extremely fast ramps, $t_{ramp} \ll J^{-1}$, do not afford the photon sufficient time to tunnel and thus the photon remains in its initial site. At intermediate ramp speeds, $t_{ramp} \approx J^{-1}$, the photon undergoes diabatic transitions to other eigenstates and thus ends up in other lattice sites, reducing the occupation of its initial site. Only slow ramps, $t_{ramp} \gg J^{-1}$, enable the photon to adiabatically follow the initial eigenstate, delocalizing and subsequently relocalizing to its initial site. It is these slowest ramps that we use for state preparation. Data points are averages of up to 11 experiments, each of which is an average of 2,000 individual measurements. Error bars reflect the s.e.m. (Supplementary Section J); in **d**, they are smaller than the markers.

Single-particle melting

Our protocol for preparing arbitrary eigenstates of a Hubbard lattice is highlighted in Fig. 1c. We begin by introducing strong disorder ($|\delta_i| \gg J$) in the lattice by controllably detuning the sites (Supplementary Section G). In this disordered configuration, tunnelling is suppressed and all eigenstates are products of localized photons on individual sites. Such states are easily prepared by injecting photons into individual sites with calibrated microwave π pulses. The lattice sites are then tuned into resonance by reducing the disorder $|\delta_i| \to 0$ slowly enough to maintain adiabaticity, allowing the system to remain in the same instantaneous eigenstate, which melts the particles into a correlated fluid. We then characterize the prepared states by site-resolved probes of occupation, coherence and correlation.

We begin by applying this preparation protocol to construction of single-photon particle-in-a-box eigenstates. The dependence of these eigenstates on disorder, and their corresponding energies, are displayed pictorially in Fig. 2a. At maximum disorder (Fig. 2a, left) each eigenstate is localized to a single site, whereas near zero disorder the eigenstates are delocalized particle-in-a-box states (Fig. 2a, right). Adiabatic evolution ensures that the system remains in the same instantaneous eigenstate, forming a unique connection between the lattice site the photon occupies in the disordered configuration and the state into which it delocalizes.

In Fig. 2b we prepare the highest energy localized states and measure the evolution of their densities as we adiabatically reduce the disorder to zero. The blue (red) data show the dynamics of a single photon prepared in the highest (second highest) energy site, Q_5 (Q_3), as it delocalizes near degeneracy. The measured density profiles of the final states are sinusoidal, with zero and one nodes, respectively, matching the probability distributions for the $q = \pi/L$ and $q = 2\pi/L$ particle-in-a-box/quasi-momentum states.

Because photon loss renders our quantum system inherently open, we must balance the need for slow evolution (set by the energy gaps)

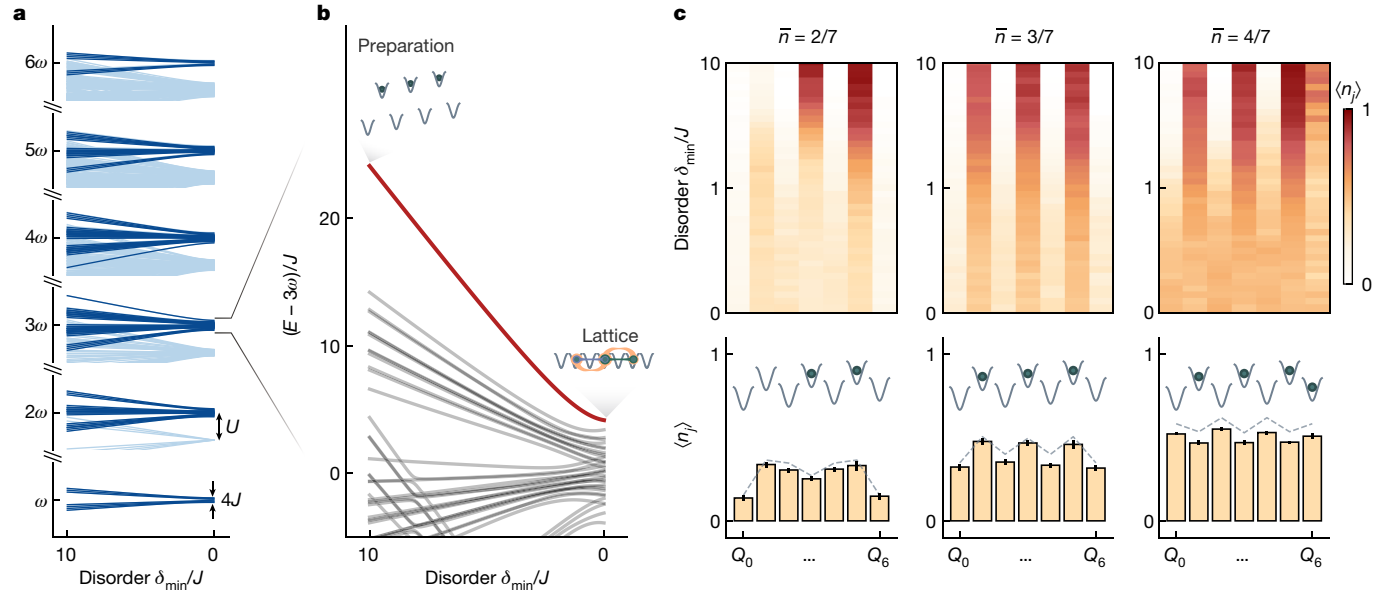

Fig. 3 | Adiabatic preparation of strongly correlated fluids of light. The ground states of the Hubbard lattice below unit filling are compressible fluids because motion of the particles is not fully blocked by collisions as it would be in the unit-filled Mott state. **a**, This is reflected in the many-body spectrum in which, in the absence of disorder, there are bands of states (dark blue) of width $\approx J$ in which the photons do not overlap with one another, rather than a single state, as would be the case for an incompressible system. These states are spectroscopically isolated by the on-site interaction U from all other states (light blue). In the incompressible Mott state there is a single gapped (by U) ground state. **b**, In the particular case of three particles in the lattice, the highest energy state, which is the fluid 'ground' state (because $U, J < 0$), exhibits the largest energy gap to all other states, and can thus be prepared most quickly. **c**, We adiabatically prepare the fluid ground states for two, three and four particles in the seven-site lattice. The upper panels display the density profiles for these states as the system is tuned from disordered to ordered configurations and the particles delocalize and become entangled. We highlight the measured fluid densities at degeneracy (bars in lower panels) compared to theory (dashed curve). The insets depict particle placements in the disordered configuration, which adiabatically connect to the fluids. Data points are averages of up to 11 experiments, each of which is an average of 2,000 measurements. Error bars reflect the s.e.m.

to satisfy adiabaticity with the need to evolve faster than photon loss. We have developed a protocol to experimentally probe the adiabaticity of the process and extract the optimum ramp rate, without needing to perform tomography on a highly entangled state: we ramp the disorder down to zero and then back up, exactly reversing the downward ramp. We then measure the fraction of the time that the photon returns to its initial lattice site. Because all eigenstates are localized in the final, disordered lattice, this is a direct measure of the overlap of the final state with the initial state $|\langle\Psi_{\text{final}}|\Psi_{\text{init}}\rangle|^2$. Performing this experiment versus total evolution time $2t_{\text{ramp}}$, provides a measure of adiabaticity.

This process is depicted in Fig. 2c for a single particle, in which it is applied to the preparation of the highest energy quasi-momentum state, as shown in Fig. 2d. For very fast ramps, $t_{\text{ramp}} \ll J^{-1}$, the photon remains in its initial site because it lacks the time to tunnel even to its nearest neighbour. For intermediate ramp speeds, $t_{\text{ramp}} \approx J^{-1}$, the photon has time to delocalize but not to adiabatically follow, and thus undergoes diabatic transitions to other quasi-momentum states as the disorder is reduced, leading to a decreased population of the initial site. When the ramp is sufficiently slow, $t_{\text{ramp}} \gg J^{-1}$, the photon is able to delocalize, adiabatically follow the same eigenstate and relocalize, resulting in near-unity occupation in the initial site. We use extensions of this technique to multiple particles (see Extended Data Fig. 1) behind the scenes to optimize performance throughout the remainder of this work. This approach is particularly powerful because it is agnostic to the details of the physical platform and target state.

Correlated fluid melting

When multiple photons simultaneously reside in our Hubbard circuit, interactions strongly modify the behaviour of the system. At unit average occupancy ($\bar{n} \equiv N/L = 1$, where N is the number of photons and L is the number of sites), the ground state is a Mott insulator[11] because the photons cannot move without immediately hitting a neighbour, so transport is fully impeded. Away from unit occupancy the ground state is a fluid: even if U fully blocks photons passing through one another, they can still delocalize, move and exchange momentum with their neighbours.

Strongly interacting fluids are challenging to prepare by reservoir engineering techniques[37], which rely on irreversible photon injection that halts when adding the next photon costs substantially more energy than prior photons. The delocalization of the photon in the fluid makes it compressible: the energy required to inject additional photons changes smoothly with density, changing abruptly only at the unit-filled Mott state.

Here we prepare a compressible, strongly correlated fluid of light away from unit filling via a multiparticle variant of our disorder-assisted preparation scheme: we determine the filling by the number of photons that we coherently inject, and the eigenstate by the sites into which we inject photons. In our $L = 7$ site lattice we inject up to $N = 6$ photons to remain below unit filling. As our interactions are attractive, $U < 0$, the 'ground' state is actually the highest energy state for a given photon number; beyond this detail, the sign of U does not impact the physics.

Figure 3a depicts the many-body spectrum for various fluid photon numbers versus disorder. The spectrum splits first into bands of fixed photon number separated by ω_0, and then into bands of fixed numbers of overlapping particles separated by the interaction energy U. Within each of these bands, the states are split by fractions of the tunnelling energy J, reflecting phonon excitations of the fluid. Fig. 3b provides a detailed view of the spectrum relevant for preparing a three-photon ground state. The preparation trajectory is highlighted, beginning in the disordered lattice with photons occupying the three highest energy sites, and ending in the ordered lattice with the photons delocalized and entangled.

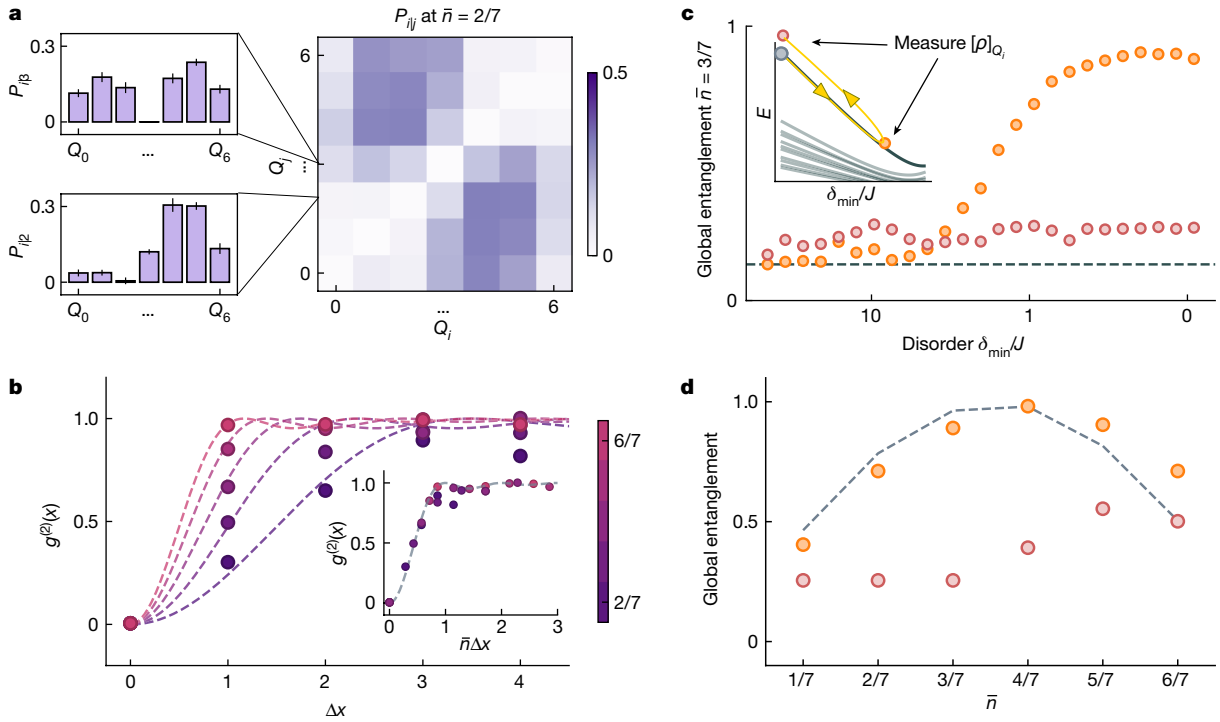

Fig. 4 | Microscopy of the strongly correlated fluid—anti-bunching and delocalization. The photon liquid is characterized by photons simultaneously (1) avoiding each other and (2) delocalizing. **a**, To show that the photons avoid one another in the fluid we measure the two-body correlator $P_{i|j}$ at $\bar{n} = \frac{2}{7}$. $P_{i|j}$ quantifies the probability of detecting a photon at site i given one detected in site j. Suppression near $i = j$ reflects both the hard-core constraint and the minimization of kinetic energy by photons smoothing their wavefunction and thus avoiding nearby sites. The upper (lower) inset showing $P_{i|3}$ ($P_{i|2}$) demonstrates that when the first photon is detected in the middle site (one site left of the middle), the second photon occupies particle-in-a-box states imposed by repulsion of the first photon. **b**, The normalized two-body correlator at various particle numbers (densities) is shown, demonstrating that the anti-correlation length decreases as the density increases, in agreement with a parameter-free Tonks–Girardeau theory (Supplementary Section F) and the intuition that photons occupy less space at higher densities. Also apparent are Friedel oscillations at wavevector $k_F = \pi\bar{n}$, signalling photon fermionization. Large-separation correlation data, polluted by edge effects, are omitted (Supplementary Fig. 7). **c**, We probe delocalization during three-particle fluid preparation by measuring the average entanglement between each site and the rest of the system, $E_{gl} \equiv 2(1 - \langle P_i \rangle)$ (orange) via the purity of the single-site reduced density operator $P_i \equiv Tr(\rho_i^2)$. In the disordered lattice, the state is a product of localized photons, thus entanglement is small. In the disorder-free lattice, photons delocalize, purity drops and entanglement increases. We distinguish environmental entanglement (decoherence) from intersite entanglement by returning to the initial configuration before measuring (red); this quantity remains small, proving the system remains unentangled with the environment. The inset depicts the measurement time within the ramp for each curve. **d**, The entanglement peaks at half-filling at which each site's occupancy provides maximal information about the rest of the system. Theoretical (dashed) particle–hole symmetry about ($\bar{n} = \frac{1}{2}$) is not reflected in the data due to increased decay with more particles (increased entanglement after reverse ramp at high densities, red). Data points are averages of up to 11 experiments, each of which is an average of 2,000 measurements. Error bars represent the s.e.m. (Supplementary Section J); where absent, they are smaller than the data points.

We perform the disorder-assisted preparation for up to four photons, measuring, in Fig. 3c, average density profiles as the lattice is tuned from disordered to disorder-free configurations (see Extended Data Fig. 2 for the case for five and six photons). These data demonstrate that during the melt the photons delocalize from their initial sites into all lattice sites, with the melted density profiles in good agreement with the disorder-free numerics from exact diagonalization.

Because we operate at large U/J, the physics is well captured by the Tonks–Girardeau model (Supplementary Section F), whose ground state is of the Bijl–Jastrow form. This wavefunction is written as the product of single- and two-particle components $\Psi_B(\mathbf{x}) = \phi(\mathbf{x})\varphi(\mathbf{x})$, for $\mathbf{x} = (x_0, x_1, \ldots, x_6)$[44]. The single-particle component $\phi(\mathbf{x}) = \prod_{i=0}^{6} \cos(\pi x_i/L)$ places each photon in the lowest energy particle-in-a-box state of the lattice, whereas the two-particle component $\varphi(\mathbf{x}) = \prod_{i<j} |x_i - x_j|$ keeps the photons apart (whilst minimizing their kinetic energy) by ramping the wavefunction to zero whenever they overlap.

In the absence of interactions, the ground-state density would be independent of particle number up to an overall scale, reflecting the single-particle eigenstate $q = \pi/L$ of Fig. 2b. The increasingly large deviations from such a sinusoidal form as density increases indicate that photon–photon collisions are shaping the fluid-density profile. A deeper understanding of the fluid's structure requires exploring correlations and entanglement, which is the subject of the remainder of this investigation.

Fluid correlations

In the Tonks regime the photon fluid should exhibit short-range repulsion between the particles arising from the Hubbard $|U| \gg J$. We probe this physics directly through the two-body correlator $P_{i|j}$, which quantifies the probability of detecting a photon at site i conditioned on one being detected at site j. If we consider a two-particle state with a wavefunction $\Psi(x_1, x_2)$, the detection of a particle at lattice site $x_1 = x_j$ collapses the wavefunction to a product state $\Psi(x_1, x_2) = \delta(x_1 - x_j)\Psi'(x_2)$, with the conditional probability of the second photon given by $P_{i|j} = |\Psi'(x_i)|^2$. This measurement is performed on a minimal two-particle fluid in Fig. 4a, where the insets show $P_{i|2}$ and $P_{i|3}$. The strong occupation suppression at $i = j$ reflects the hard-core constraint that forces the system wavefunction to vanish when two particles are on top of each other. Furthermore, the suppression near $i = j$ reflects the

preference of the photons to minimize their wavefunction curvature and thus their kinetic energy. The projective measurement of a photon in the lattice has effectively reshaped the two-particle fluid into a single-particle fluid confined in 'two' boxes, in which the pinned (detected) photon acts as a potential barrier for the second photon.

To probe two-body correlations in fluids of more than two photons, we measure the system-averaged, normalized two-body correlator given by:

$$g^{(2)}(x) = \frac{1}{\bar{n}^2} \sum_i \langle n_i n_{i+x} \rangle,$$

which quantifies the probability of simultaneously detecting two particles separated by x (in lattice sites), normalized to the average density $\bar{n}$. The central intuition, that each photon has less 'space' at higher densities, is captured in Fig. 4b, in which the anti-bunched region ($g^{(2)}(x) < 1$) gets narrower as density increases. Indeed, when the separation is rescaled by the density, the correlator collapses onto a universal parameter-free Tonks–Girardeau theory, with each particle occupying a volume $1/\bar{n}$, and characteristic Friedel oscillations. These correlations, oscillating at the Fermi momentum, $k_F = \pi\bar{n}$, are a direct signature of the 'fermionization' of the photons[13].

Fluid delocalization and entanglement

As the photons melt into a fluid they optimize their energy by delocalizing as much as possible whilst avoiding one another. The two-body correlator explored in the previous section quantifies this avoidance, and in this section we explore their delocalization. To achieve this we probe the entanglement of a single site with the remainder of the system by using a metric developed for interacting spins[45]: we measure the reduced density matrix of each individual lattice site ρ_i, quantifying how strongly it is entangled with the rest of the lattice from its impurity $1 - \mathrm{Tr}(\rho_i^2)$. Our global measure of multipartite entanglement/delocalization is this impurity averaged over all sites:

$$E_{\mathrm{gl}} = 2 - \frac{2}{N} \sum_{i=1}^{N} \mathrm{Tr}(\rho_i^2).$$

We wish to understand how the global entanglement scales with the number of particles and lattice disorder, which dictates the degree of delocalization. In Fig. 4c the entanglement is measured for a three-particle fluid as we vary the disorder along the adiabatic preparation trajectory. In the limit of strong lattice disorder the entanglement between sites is very small, as the three-particle state is a product of localized photons. As we reduce the disorder, the entanglement grows, saturating to a maximum value when the sites are degenerate and the photons become fully delocalized. Residual entanglement in the disordered lattice arises from dissipative coupling to the environment, that is, decoherence. We exclude the possibility that decoherence is the source of entanglement in the fluid phase by ramping the lattice back to its initial disordered configuration. The fact that the measured entanglement drops definitively proves that the entanglement observed at degeneracy comes from delocalization, and not dissipation. Similar measurements and conclusions are extracted for all the other particle sectors (Extended Data Fig. 3).

The dependence of the entanglement at degeneracy on the average density is displayed, together with the expected theoretical calculation, in Fig. 4d. The discrepancy at larger filling fractions is due to increased particle loss, as anticipated from the increased entanglement after the time-reversed ramp. As highlighted in the theory, there is a particle–hole symmetry in the extracted entanglement measure. This is expected because in the hard-core limit, particles at filling $\bar{n}$ tunnel and avoid one another analogously to holes at filling $1 - \bar{n}$. Entanglement is maximized at half-filling because that is the situation in which knowledge of the occupancy of any given site provides the 'most' information about the occupancy of adjacent sites: at lower (higher) fillings, most sites are empty (occupied), so knowledge of any given site's occupancy provides less information.

Outlook

In this work we have demonstrated a way to harness controlled disorder to individually index and prepare the eigenstates of a strongly interacting many-body system. In particular, we have assembled quantum fluids of light in a 1D Bose–Hubbard circuit composed of capacitively coupled transmon qubits. Leveraging our site-resolved tuning capabilities, we tune the qubits out of resonance with one another, individually excite only particular qubits and then melt these excitations into a fluid. Site-resolved probes of correlation, entanglement and reversibility reveal that this system realizes a Tonks–Girardeau gas[12,13]. The dissipative stabilization technique of ref. [11] will yield lower entropy per particle when many-body gaps are large, but the gaps at the critical point are small; the approach demonstrated here is preferable when the phase is compressible, so dissipative stabilization will be unable to stabilize a specific particle number. Leveraging both techniques, the Bose–Hubbard circuit is now prepared to study most phases of quantum matter. It remains to be seen how our adiabatic preparation approach scales with system size; it seems certain that it will be controlled by the Kibble–Zurek mechanism[46] in the thermodynamic limit, although the precise disorder used will probably affect the structure of the excitations generated at the critical point.

By combining the techniques developed in this work with topological[29,47] circuit lattices, it should be possible to prepare topological fluids of light[5]. In conjunction with auxiliary qubits, these adiabatic preparation techniques will enable direct measurements of out-of-time-order correlators and information scrambling[48], as well as anyon statistics[49].

Online content

Any methods, additional references, Nature Portfolio reporting summaries, source data, extended data, supplementary information, acknowledgements, peer review information; details of author contributions and competing interests; and statements of data and code availability are available at https://doi.org/10.1038/s41586-022-05357-x.

1. Laflamme, R., Miquel, C., Paz, J. P. & Zurek, W. H. Perfect quantum error correcting code. *Phys. Rev. Lett.* **77**, 198–201 (1996).
2. Devitt, S. J., Munro, W. J. & Nemoto, K. Quantum error correction for beginners. *Rep. Prog. Phys.* **76**, 076001 (2013).
3. Carusotto, I. et al. Photonic materials in circuit quantum electrodynamics. *Nat. Phys.* **16**, 268–279 (2020).
4. Pezze, L., Smerzi, A., Oberthaler, M. K., Schmied, R. & Treutlein, P. Quantum metrology with nonclassical states of atomic ensembles. *Rev. Mod. Phys.* **90**, 035005 (2018).
5. Grusdt, F., Letscher, F., Hafezi, M. & Fleischhauer, M. Topological growing of Laughlin states in synthetic gauge fields. *Phys. Rev. Lett.* **113**, 155301 (2014).
6. Dallaire-Demers, P.-L., Romero, J., Veis, L., Sim, S. & Aspuru-Guzik, A. Low-depth circuit ansatz for preparing correlated fermionic states on a quantum computer. *Quantum Sci. Technol.* **4**, 045005 (2019).
7. Kapit, E., Hafezi, M. & Simon, S. H. Induced self-stabilization in fractional quantum Hall states of light. *Phys. Rev. X* **4**, 031039 (2014).
8. Lebreuilly, J. et al. Stabilizing strongly correlated photon fluids with non-Markovian reservoirs. *Phys. Rev. A* **96**, 033828 (2017).
9. Albash, T. & Lidar, D. A. Adiabatic quantum computation. *Rev. Mod. Phys.* **90**, 015002 (2018).
10. Zurek, W. H., Dorner, U. & Zoller, P. Dynamics of a quantum phase transition. *Phys. Rev. Lett.* **95**, 105701 (2005).
11. Ma, R. et al. A dissipatively stabilized Mott insulator of photons. *Nature* **566**, 51–57 (2019).
12. Tonks, L. The complete equation of state of one, two and three-dimensional gases of hard elastic spheres. *Phys. Rev.* **50**, 955–963 (1936).
13. Girardeau, M. Relationship between systems of impenetrable bosons and fermions in one dimension. *J. Math. Phys.* **1**, 516–523 (1960).
14. Goldman, N., Budich, J. C. & Zoller, P. Topological quantum matter with ultracold gases in optical lattices. *Nat. Phys.* **12**, 639–645 (2016).
15. Ozawa, T. et al. Topological photonics. *Rev. Mod. Phys.* **91**, 015006 (2019).
16. Blatt, R. & Roos, C. F. Quantum simulations with trapped ions. *Nat. Phys.* **8**, 277–284 (2012).
17. Bloch, I., Dalibard, J. & Nascimbene, S. Quantum simulations with ultracold quantum gases. *Nat. Phys.* **8**, 267–276 (2012).

18. Clark, L. W., Schine, N., Baum, C., Jia, N. & Simon, J. Observation of Laughlin states made of light. *Nature* **582**, 41–45 (2020).
19. Chen, Q., Stajic, J., Tan, S. & Levin, K. BCS–BEC crossover: from high temperature superconductors to ultracold superfluids. *Phys. Rep.* **412**, 1–88 (2005).
20. Greiner, M., Mandel, O., Esslinger, T., Hänsch, T. W. & Bloch, I. Quantum phase transition from a superfluid to a Mott insulator in a gas of ultracold atoms. *Nature* **415**, 39–44 (2002).
21. Cooper, N., Dalibard, J. & Spielman, I. Topological bands for ultracold atoms. *Rev. Mod. Phys.* **91**, 015005 (2019).
22. Bakr, W. S., Gillen, J. I., Peng, A., Fölling, S. & Greiner, M. A quantum gas microscope for detecting single atoms in a Hubbard-regime optical lattice. *Nature* **462**, 74–77 (2009).
23. Trotzky, S. et al. Time-resolved observation and control of superexchange interactions with ultracold atoms in optical lattices. *Science* **319**, 295–299 (2008).
24. Islam, R. et al. Measuring entanglement entropy in a quantum many-body system. *Nature* **528**, 77–83 (2015).
25. Karamlou, A. H. et al. Quantum transport and localization in 1d and 2d tight-binding lattices. *npj Quantum Inform.* **8**, 35 (2022).
26. Zhang, J. et al. Observation of a discrete time crystal. *Nature* **543**, 217–220 (2017).
27. Choi, S. et al. Observation of discrete time-crystalline order in a disordered dipolar many-body system. *Nature* **543**, 221–225 (2017).
28. Choi, J.-Y. et al. Exploring the many-body localization transition in two dimensions. *Science* **352**, 1547–1552 (2016).
29. Roushan, P. et al. Spectroscopic signatures of localization with interacting photons in superconducting qubits. *Science* **358**, 1175–1179 (2017).
30. Bluvstein, D. et al. Controlling quantum many-body dynamics in driven Rydberg atom arrays. *Science* **371**, 1355–1359 (2021).
31. Brown, P. T. et al. Bad metallic transport in a cold atom Fermi–Hubbard system. *Science* **363**, 379–382 (2019).
32. McIver, J. W. et al. Light-induced anomalous Hall effect in graphene. *Nat. Phys.* **16**, 38–41 (2020).
33. Choi, S., Bao, Y., Qi, X.-L. & Altman, E. Quantum error correction in scrambling dynamics and measurement-induced phase transition. *Phys. Rev. Lett.* **125**, 030505 (2020).
34. Eisert, J., Friesdorf, M. & Gogolin, C. Quantum many-body systems out of equilibrium. *Nat. Phys.* **11**, 124–130 (2015).
35. Simon, J. et al. Quantum simulation of antiferromagnetic spin chains in an optical lattice. *Nature* **472**, 307–312 (2011).
36. Mazurenko, A. et al. A cold-atom Fermi–Hubbard antiferromagnet. *Nature* **545**, 462–466 (2017).
37. Ma, R., Owens, C., Houck, A., Schuster, D. I. & Simon, J. Autonomous stabilizer for incompressible photon fluids and solids. *Phys. Rev. A* **95**, 043811 (2017).
38. Bak, P. Commensurate phases, incommensurate phases and the devil's staircase. *Rep. Prog. Phys.* **45**, 587 (1982).
39. Umucalílar, R., Simon, J. & Carusotto, I. Autonomous stabilization of photonic Laughlin states through angular momentum potentials. *Phys. Rev. A* **104**, 023704 (2021).
40. Gemelke, N., Zhang, X., Hung, C.-L. & Chin, C. In situ observation of incompressible Mott-insulating domains in ultracold atomic gases. *Nature* **460**, 995–998 (2009).
41. Zhou, Y., Kanoda, K. & Ng, T.-K. Quantum spin liquid states. *Rev. Mod. Phys.* **89**, 025003 (2017).
42. Kinoshita, T., Wenger, T. & Weiss, D. S. Observation of a one-dimensional Tonks–Girardeau gas. *Science* **305**, 1125–1128 (2004).
43. Paredes, B. et al. Tonks–Girardeau gas of ultracold atoms in an optical lattice. *Nature* **429**, 277–281 (2004).
44. Cazalilla, M. A., Citro, R., Giamarchi, T., Orignac, E. & Rigol, M. One dimensional bosons: from condensed matter systems to ultracold gases. *Rev. Mod. Phys.* **83**, 1405–1466 (2011).
45. Meyer, D. A. & Wallach, N. R. Global entanglement in multiparticle systems. *J. Math. Phys.* **43**, 4273 (2002).
46. Chandran, A., Erez, A., Gubser, S. S. & Sondhi, S. L. Kibble–Zurek problem: universality and the scaling limit. *Phys. Rev. B* **86**, 064304 (2012).
47. Owens, J. C. et al. Chiral cavity quantum electrodynamics. *Nat. Phys.* **18**, 1048–1052 (2022).
48. Swingle, B., Bentsen, G., Schleier-Smith, M. & Hayden, P. Measuring the scrambling of quantum information. *Phys. Rev. A* **94**, 040302 (2016).
49. Grusdt, F., Yao, N. Y., Abanin, D., Fleischhauer, M. & Demler, E. Interferometric measurements of many-body topological invariants using mobile impurities. *Nat. Commun.* **7**, 11994 (2016).
50. Koch, J. et al. Charge-insensitive qubit design derived from the Cooper pair box. *Phys. Rev. A* **76**, 042319 (2007).

Methods

Device fabrication

The 10×20 mm^2 chip was fabricated in a two-step lithography process. Optical lithography was used to generate a 200 nm thick tantalum layer covering in-plane features of size >1 μm, and a second e-beam lithography step enabled deposition of smaller Al/AlO_x/Al Josephson junctions atop the sapphire substrate. Detailed information on the fabrication process can be found in Supplementary Section A.

Device parameters

To generate the Bose–Hubbard Hamiltonian for microwave photons we fabricated a 1D chain of capacitively coupled transmon qubits, creating a nearest-neighbour tunnelling energy $J \approx 2\pi \times 9$ MHz between the qubit lattice sites and made use of the nonlinearity of the qubits to generate strong interactions between photons $U \approx 2\pi \times 250$ MHz. Each transmon lattice site was capacitively coupled to a linear resonator and filter (Supplementary Section D), which we probed (Supplementary Section E) to determine the state of the connected qubit. To converge to these parameters we used finite element simulation techniques, mainly HFSS, in the design phase and iterated changes on the basis of experimental measurements. A table of system parameters for the entire sample can be found in Supplementary Section I.

Microwave wiring

The sample was mounted and wire bonded to a copper PCB, which was mounted in shielding consisting of copper, MuMetal and lead to prevent radiation interacting with the sample. The shielded sample was mounted to the mixing chamber plate of a dilution refrigerator to cool the sample below T_c to 9 mK. Microwave coaxial cables and d.c. twisted-pair wires fed signals from a room-temperature homodyne measurement setup (Supplementary Fig. 1) into the shielded sample. We corrected distortions of signals sent to the qubit from the wiring and filters by inverting the transfer function and pre-applying a kernel to the signal (Supplementary Section H).

Flux bias and crosstalk

By sending d.c. currents near the SQUID loop of the transmon qubits we biased the local magnetic field and enabled tuning of qubit frequencies of approximately 4–6 GHz, which we used to introduce disorder $\delta_i \gg J$ to the array. This localized the eigenstates of the now disordered system to excitations on single sites, which we selectively populated by driving power at that frequency using the common feedline. The mutual inductance we observed between one qubit's flux line and another qubit's SQUID loop defines a parasitic crosstalk, which we addressed by inverting a measured crosstalk matrix and applying linear corrections to additional residual error (Supplementary Section G). An additional global solenoid near the sample was used to gain an additional degree of freedom to bias the qubits and minimize the thermal load at the refrigerator needed to run experiments.

Pulse sequence

Initially our lattice started in a strongly disordered configuration $|\delta_i| > U$, then we jumped to a $|\delta_i| < U$ configuration and applied excitations to transmon lattice sites to avoid further Landau–Zener processes during state preparation (Supplementary Section C). We then adiabatically removed the remaining disorder to selectively generate the desired compressible fluid states on the disorder-free lattice. To optimize performance of the adiabatic trajectory in state preparation we optimized reversibility of the trajectory: $|\langle\psi_i|\psi_f\rangle|^2$ (Fig. 2d and Extended Data Fig. 1).

Readout

To readout the state of the lattice we probed the response of radiofrequency signals sent down into the common feedline at the frequency of the dispersively coupled readout resonators. To extract qubit populations in the $|0\rangle$ and $|1\rangle$ states in this regime we probed at two separate frequencies, which maximally distinguish the qubit states $|0\rangle$ from $|1\rangle$, $|2\rangle$ and $|1\rangle$ from $|0\rangle$, $|2\rangle$ and assume population lies within only these three states. We used a confusion matrix to correct for errors in binning, with additional errors stemming from readout crosstalk and Landau–Zener processes (Supplementary Section E).

Experimental results

We measured the assembly of single and multiparticle fluid eigenstates by measuring the population across all lattice sites, sampled across the parameterized removal of disorder δ_i (Figs. 2b and 3c). To characterize the physics of particle interaction in states with $n \geq 2$ photons, we measured the two-body correlator given by the conditional measurement P_{ij} (Fig. 4c) and function $g^2(x)$ (Fig. 4d), in which interactions influence the shape of the remaining one-particle wavefunction after measurement and the latter reveals variation in anti-bunching across densities. These results coincide with a parameter-free Tonks–Girardeau model (Supplementary Section F). We measured delocalization of the compressible fluid states ($\bar{n} = \frac{1}{7} - \frac{6}{7}$) as disorder was removed via the global entanglement entropy. Figure 4d shows our results for $\bar{n} = \frac{3}{7}$, whereas measurements and theory results for global entanglement across the adiabatic disorder sweep for all densities are displayed in Extended Data Fig. 3.

Data availability

The experimental data presented in this manuscript are available from the corresponding author upon request, due to the proprietary file formats used in the data collection process.

Code availability

The source code for simulations throughout are available from the corresponding author upon request.

Acknowledgements This work was supported by ARO MURI grant W911NF-15-1-0397, AFOSR MURI grant FA9550-19-1-0399 and by NSF Eager grant 1926604. Support was also provided by the Chicago MRSEC, which is funded by NSF through grant DMR-1420709. G.R. and M.G.P. acknowledge support from the NSF GRFP. A.V. acknowledges support from the MRSEC-funded Kadanoff–Rice Postdoctoral Research Fellowship. Devices were fabricated in the Pritzker Nanofabrication Facility at the University of Chicago, which receives support from Soft and Hybrid Nanotechnology Experimental (SHyNE) Resource (NSF ECCS-1542205), a node of the National Science Foundation's National Nanotechnology Coordinated Infrastructure.

Author contributions The experiments were designed by B.S., A.V., G.R., J.S. and D.I.S. The apparatus was built by B.S., A.V. and G.R. The collection of data was handled by B.S., A.V. and G.R. All authors analysed the data and contributed to the manuscript.

Competing interests The authors declare no competing interests.

Additional information
Supplementary information The online version contains supplementary material available at https://doi.org/10.1038/s41586-022-05357-x.
Correspondence and requests for materials should be addressed to Brendan Saxberg.
Peer review information *Nature* thanks the anonymous reviewers for their contribution to the peer review of this work.

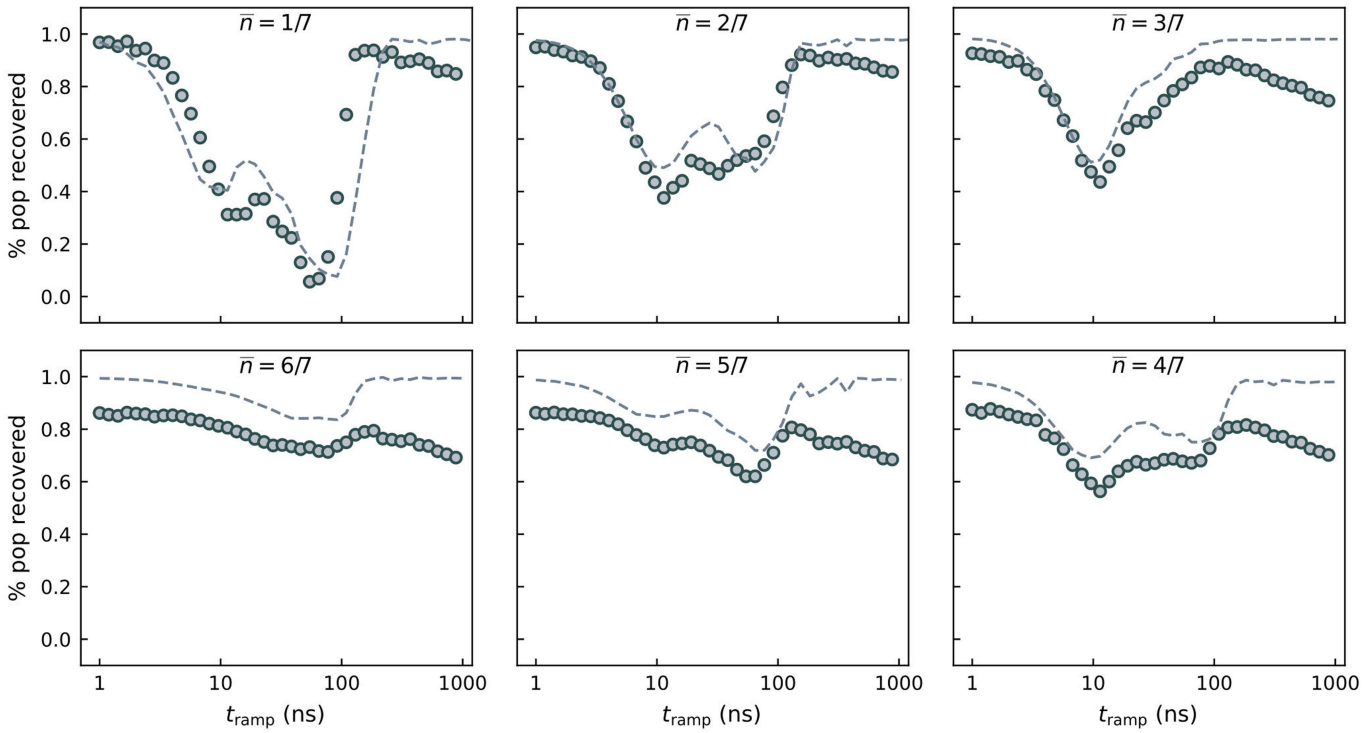

Extended Data Fig. 1 | Adiabaticity Curves for All $\bar{n}$ Fillings. Adiabaticity is given by the average number of photons that return to the originally excited sites as a function of ramp length. Here, we measure adiabaticity curves for the highest energy eigenstate for all $\bar{n}$ fillings, revealing the minimum ramp length needed to be adiabatic when preparing these many-body states. As particle number increases, we start to suffer more from loss and no longer fully recover the initial starting population.

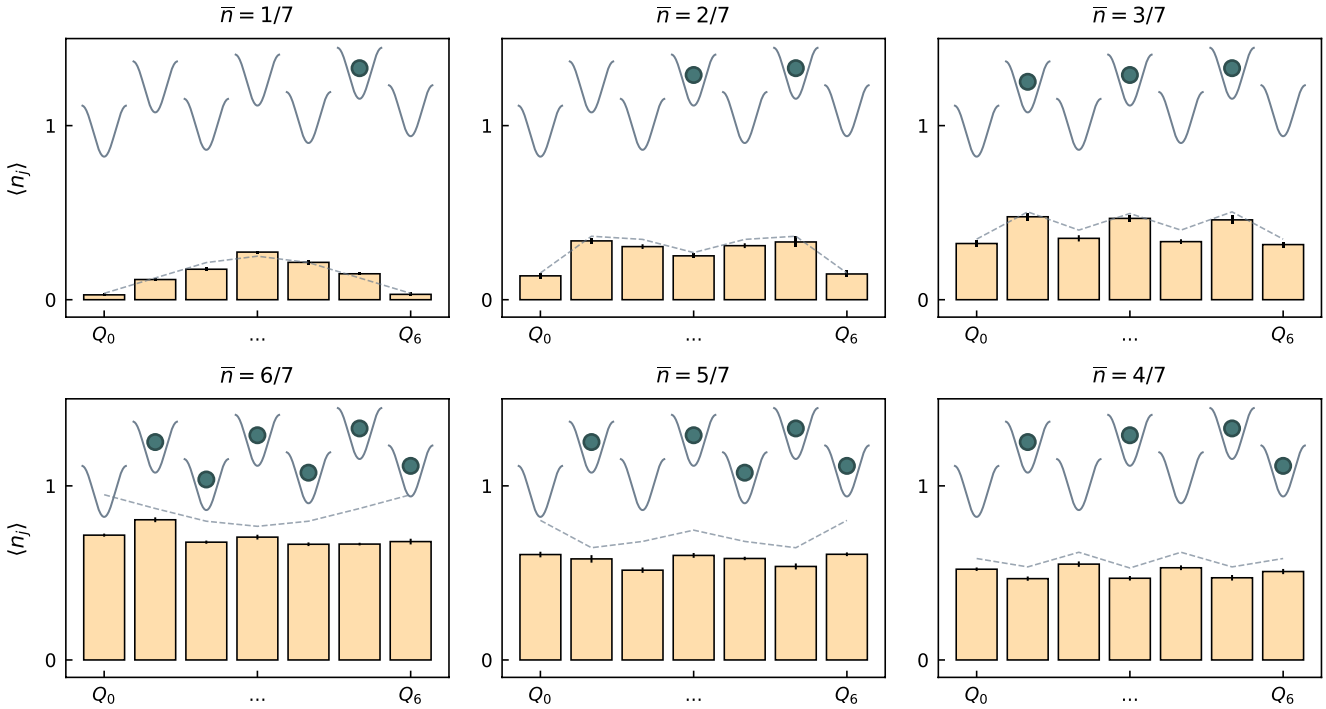

Extended Data Fig. 2 | Profiles for $\overline{n}$ Fillings. Density profiles for the highest energy eigenstates, corresponding to fluid ground states, for filling $\overline{n}=\frac{1}{7}$ through $\frac{6}{7}$. For 5 and 6 particles, our results suffer from particle loss.

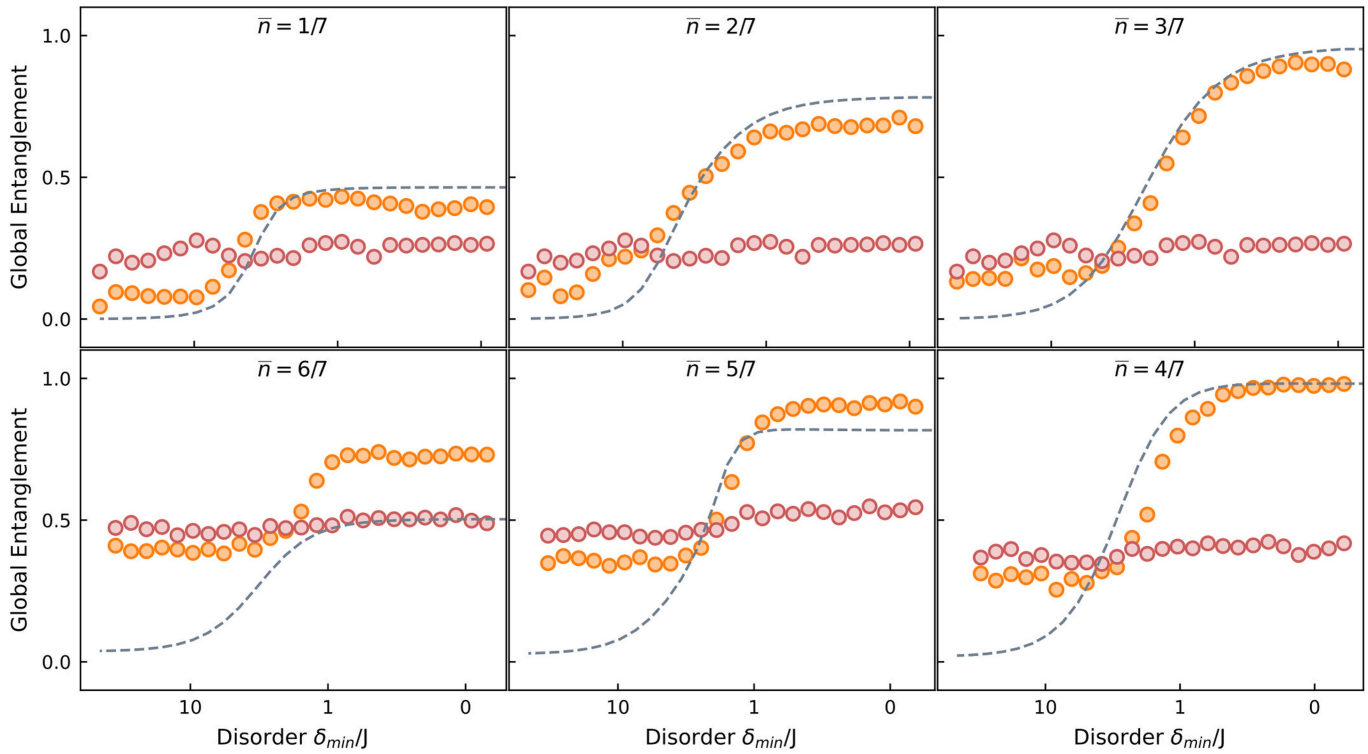

Extended Data Fig. 3 | Entanglement for $\bar{n}$ Fillings. Measure of entanglement vs disorder, for filling $\bar{n}$=$\frac{1}{7}$ through $\frac{6}{7}$. Error bars reflect S.E.M.; here they are smaller than markers.